International Journal of Multiphase Flow 139 (2021) 103566

Contents lists available at ScienceDirect

International Journal of Multiphase Flow

journal homepage: www.elsevier.com/locate/ijmulflow

Particle Reynolds number effects on settling ellipsoids in isotropic turbulence

Konstantin Fröhlich[a,*], Pooria Farmand[b], Heinz Pitsch[b], Matthias Meinke[a,c], Wolfgang Schröder[a,c]

[a] Institute of Aerodynamics, RWTH Aachen University, Wüllnerstr. 5a, Aachen 52062, Germany
[b] Institute for Combustion Technology, RWTH Aachen University, Templergraben 64, Aachen 52056, Germany
[c] JARA-CSD, RWTH Aachen University, Aachen 52074, Germany

ARTICLE INFO

Article history:
Received 8 October 2020
Revised 21 December 2020
Accepted 15 January 2021
Available online 24 February 2021

Keywords:
Non-spherical particles
Turbulent flow
Euler-Lagrange model
Gas-solid suspension

ABSTRACT

Recently developed drag correlations for ellipsoidal particles are applied in a Lagrangian point-particle model. The results are directly compared against a popular Lagrangian model based on the dynamic equations valid for Stokes flow for the canonical case of settling ellipsoids in isotropic decaying turbulence. For increasing terminal velocities, the pitching torque due to fluid inertia dominates the torque contribution due to the fluid velocity gradient. Consequently, the major axis is preferentially oriented perpendicular to the settling direction. The opposite is predicted, if the new correlations for ellipsoidal particles are not included in the Lagrangian model. The combined effect of the pitching torque and the drag correlations leads to significantly different settling velocities for the varying correlations. The results based on a constant particle relaxation time for various particle diameters show that the particle Reynolds number is a relevant parameter in a multiphase system even for relatively moderate particle Reynolds numbers $Re_p \leq 4$.

1. Introduction

The simulation of particle-laden turbulent flows requires accurate and efficient models for the solid phase. A popular model for the particle phase is the point-particle method, where the fluid-particle interaction is not directly resolved. The particles are tracked in a Lagrangian frame via model functions for the force and the torque. The model functions define the accuracy and reliability of the point-particle method. Due to a wide variety of applications specialized formulations of model functions for the particle dynamics have been proposed and applied in the literature. For example, a quite mature model function for small solid spherical particles in non-uniform flows has been proposed by Maxey and Riley (1983). This model takes into account pressure gradients in the flow field, the added mass forces, buoyancy, history forces, gravity, and the quasi-steady Stokes drag. For solid-gas suspensions with high density ratios, it has been repeatedly confirmed that gravity forces and the Stokes drag dominate the particle dynamics such that the remaining force terms are often neglected (Kuerten, 2016; Balachandar and Eaton, 2010).

In contrast to spherical particles, the models for particle dynamics of ellipsoids are strongly limited. Model functions for the force and the torque acting on non-spherical particles are only available for specific parameter configurations which are presented next with focus on the settling of ellipsoids in turbulent flows. The existing model functions for heavy inertial particles can be classified into three categories:

- analytical solutions for creeping flow conditions, i.e., for particle Reynolds numbers $Re_p \to 0$
- analytical fluid inertia corrections for $Re_p \ll 1$
- empirical correlations for particle Reynolds number $Re_p > 0$

The first category is based on the dynamic equations derived by Jeffery (1922). It is frequently applied and quite established especially for turbulent wall-bounded flows (Marchioli et al., 2016; Marchioli and Soldati, 2013; Mortensen et al., 2008). For settling prolate ellipsoids with aspect ratios $\beta > 1$ suspended in turbulent flows, the model predicts that the major axes of the particles are preferentially aligned with the gravity direction and an increased settling velocity compared to randomly oriented particles is observed in, e.g., Siewert et al., 2014; Challabotla et al. (2016). This trend is more pronounced for higher settling velocities.

First analytical extensions of the dynamic equations for creeping flow conditions by leading order fluid inertia corrections

* Corresponding author.
E-mail address: k.froehlich@aia.rwth-aachen.de (K. Fröhlich).

https://doi.org/10.1016/j.ijmultiphaseflow.2021.103566
0301-9322/

for nearly spherical particles have been proposed in Cox (1965). Later, corrections for fibres with high aspect ratios have been proposed by Khayat and Cox (1989) and experimentally validated by Lopez and Guazzelli (2017) and Roy et al. (2019). Similar corrections have been introduced for spheroidal particles with arbitrary aspect ratios by Dabade et al. (2015). In the case of settling ellipsoids in turbulent flows, it was estimated by Sheikh et al. (2020) that an additional fluid inertia torque contribution dominates the viscous terms due to fluid velocity gradients. Consistently with earlier estimates for nearly spherical particles (Klett, 1995), this model predicts that the particles have preferentially a horizontal orientation which is opposite to the predictions without fluid inertia effects (Gustavsson et al., 2019).

Most of the aforementioned studies were motivated by atmospheric multiphase flows such as ice crystals suspended in clouds. However, in many technical environments like in pulverized biomass combustion, the relatively strict condition $Re_p \ll 1$ is not fulfilled and analytical fluid inertia corrections can not be applied. To extend the parameter space, empirical correlations are included in the Lagrangian models to account for fluid inertia effects (Voth and Soldati, 2017). Such correlations have been proposed for non-spherical particle shapes in, e.g., Zastawny et al. (2012) and Ouchene et al. (2016). These correlations are empirical functions which have been developed by linear regression for drag, lift, and torque data based on parameter studies for the simplified setup of uniform flow past inclined ellipsoids. The correlations have been applied in particle-laden turbulent channel flow by van Wachem et al. (2015) and by Arcen et al. (2017). A wall-normal gravity force acting on the particles was specified for a horizontal configuration by van Wachem et al. (2015) and it was observed that the particles have a preferred orientation with their major axis perpendicular to the relative velocity between the particle and the fluid. For a a vertical configuration with a wall-parallel gravity direction, it was observed by Arcen et al. (2017), that the particles are preferentially aligned with the settling direction in the channel center. It is not clear, if the contradicting trend of the particle orientation observed in the studies by van Wachem et al. (2015) and Arcen et al. (2017) can be explained by the different numerical setups.

Further studies are required to examine, if the particle orientations of settling ellipsoids predicted by correlations are consistent with the estimates of (Sheikh et al., 2020) and the simulations of Gustavsson et al. (2019) based on fluid inertia corrections for $Re_p \ll 1$. This motivates the current study where the settling of ellipsoidal particles is investigated via a Lagrangian point-particle model using drag correlations for $Re_p > 0$. Since existing drag correlations for ellipsoids were not convincing (Andersson and Jiang, 2019), novel correlations have been recently derived by Fröhlich et al. (2020). They are based on the regression of a large parameter study where about 4400 highly resolved direct particle-fluid simulations of ellipsoids in uniform flow were performed for the parameter space $1 \leq \beta \leq 8$ and $Re_p \leq 100$. In the current study, the correlations are directly included into an existing ellipsoidal Lagrangian point-particle model based on the dynamic equations of creeping flow conditions. Consistently with previous studies performed in, e.g., Fröhlich et al. (2018), and Schneiders et al. (2019), isotropic decaying turbulence serves as a canonical flow configuration without artificial forcing. In contrast to the studies of van Wachem et al. (2015) and Arcen et al. (2017), the particle dynamics predicted without and with correlations are directly compared to assess the impact of the correlations on the results. Additionally, particle Reynolds number effects and the importance of the drag correlations on the settling dynamics of the particles are investigated.

The structure of the manuscript is as follows. First, the mathematical model for the fluid phase is briefly presented. Then, the dynamic equations of the ellipsoidal particles are introduced which are applied in the Lagrangian point-particle method, and the correlations for drag, lift, and torque for $Re_p > 0$ are discussed. Subsequently, the discretization based of a numerical framework for low Mach number compressible flow problems as well as the computational setup are introduced. Finally, the results are presented, before the essential findings are summarized.

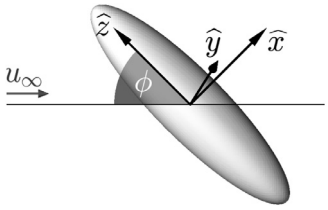

Fig. 1. Particle-fixed coordinate system $(\widehat{x}, \widehat{y}, \widehat{z})$ with the inclination angle ϕ.

2. Mathematical model

2.1. Equations governing the fluid motion

The conservation of mass, momentum, and energy is considered in a fixed control volume V by

$$\frac{d}{dt}\int_V \rho \, dV + \oint_{\partial V} [\rho \boldsymbol{u}] \cdot \boldsymbol{n} \, dA = 0, \tag{1a}$$

$$\frac{d}{dt}\int_V \rho \boldsymbol{u} \, dV + \oint_{\partial V} [\rho \boldsymbol{u}\boldsymbol{u} + p\underline{\boldsymbol{I}} - \underline{\boldsymbol{\tau}}] \cdot \boldsymbol{n} \, dA = \boldsymbol{0}, \tag{1b}$$

$$\frac{d}{dt}\int_V \rho E \, dV + \oint_{\partial V} [\rho E \boldsymbol{u} + p\boldsymbol{u} - \underline{\boldsymbol{\tau}} \cdot \boldsymbol{u} + \boldsymbol{q}] \cdot \boldsymbol{n} \, dA = 0, \tag{1c}$$

with the density ρ, the velocity vector $\boldsymbol{u}$, the pressure p, the unit tensor $\underline{\boldsymbol{I}}$, and the outward-facing unit normal vector $\boldsymbol{n}$ of the control volume surface ∂V. For a Newtonian fluid with vanishing bulk viscosity, the stress tensor is given by Aris (2012)

$$\underline{\boldsymbol{\tau}} = 2\mu \underline{\boldsymbol{S}} - \frac{2}{3}\mu(\nabla \cdot \boldsymbol{u})\underline{\boldsymbol{I}}, \tag{2}$$

with the rate-of-strain tensor $\underline{\boldsymbol{S}} = [\nabla \boldsymbol{u} + (\nabla \boldsymbol{u})^T]/2$. The dynamic viscosity μ and the thermal conductivity k are computed as a function of the temperature T by Sutherland's law (White, 1991). The equations are closed by the ideal gas equation and Fourier's law for the heat conduction $\boldsymbol{q}$.

2.2. Equations governing the particle motion

The particles are tracked via an ellipsoidal Lagrangian model in the global frame whereas the dynamic equations are solved in the particle-fixed coordinate system $(\widehat{x}, \widehat{y}, \widehat{z})$ depicted in Fig. 1. The orientation of the particle frame is described using quaternions (Siewert et al., 2014) and the geometry of the ellipsoid is defined by the minor semi-axis a and the major semi-axis $c = \beta a$. To include the correlations, the conventional notation for the translational dynamics of an ellipsoidal particle in Stokes flow as in, e.g., Happel and Brenner (2012), is reformulated. The force acting on the ellipsoid is decomposed in a drag contribution and a lift contribution with the directions $\widehat{\boldsymbol{d}}_D$ and $\widehat{\boldsymbol{d}}_L$ defined in the particle-fixed coordinate system by

$$\widehat{\boldsymbol{d}}_D = \frac{\widehat{\boldsymbol{u}} - \widehat{\boldsymbol{v}}_p}{|\widehat{\boldsymbol{u}} - \widehat{\boldsymbol{v}}_p|}, \tag{3}$$

$$\widehat{\boldsymbol{d}}_L = \widehat{\boldsymbol{d}}_D \times \widehat{\boldsymbol{d}}_T, \tag{4}$$

$$\widehat{\boldsymbol{d}}_T = \frac{\widehat{\boldsymbol{d}}_D \times \widehat{\boldsymbol{e}}_3}{|\widehat{\boldsymbol{d}}_D \times \widehat{\boldsymbol{e}}_3|} \operatorname{sgn}(\widehat{\boldsymbol{d}}_D \cdot \widehat{\boldsymbol{e}}_3), \tag{5}$$

with the fluid and the particle velocities $\widehat{\boldsymbol{u}}, \widehat{\boldsymbol{v}}_p$, the direction of the pitching torque $\widehat{\boldsymbol{d}}_T$, and the unit basis vector $\widehat{\boldsymbol{e}}_3 = (0, 0, 1)^T$ denoting the direction of the major axis of the ellipsoid. The acceleration of an ellipsoid subject to gravity $\boldsymbol{g}$ is given by

$$\frac{d\widehat{\boldsymbol{v}}}{dt} = \widehat{\boldsymbol{g}} + \frac{Re_p}{\tau_p} \frac{|\widehat{\boldsymbol{u}} - \widehat{\boldsymbol{v}}_p|}{24} \left(C_{D,\phi}(Re_p, \beta) \widehat{\boldsymbol{d}}_D + C_{L,\phi}(Re_p, \beta) \widehat{\boldsymbol{d}}_L \right), \tag{6}$$

with the particle relaxation time $\tau_p = 2\rho_p r_{eq}^2/(9\mu)$ of a sphere with the volume equivalent radius $r_{eq} = a(\beta)^{1/3}$ of the ellipsoid and the particle density ρ_p. The particle acceleration is governed by the orientation-dependent drag and lift coefficients $C_{D,\phi}$ and $C_{L,\phi}$. Two sets of drag and lift coefficients are applied in this study and the results are compared with each other. The first set is based on the solution for creeping flow conditions and referred to as Lagrangian model without correlations. Although the dynamic equations have been reformulated, they are identical to the ellipsoidal Lagrangian model for Stokes flow for $\beta > 1$ as presented in, e.g., Mortensen et al., 2008; Marchioli and Soldati (2013). In the second set, the drag and lift coefficients are extended by empirical drag correlations which have been derived in Fröhlich et al. (2020). In this study, a large data basis has been generated for drag, lift, and torque via highly-resolved simulations of inclined ellipsoids in uniform flow. A regression of the data base has been performed to derive empirical drag, lift, and torque correlations. These correlations converge to the results of Stokes flow for $Re_p \to 0$, and otherwise correct the drag and lift forces for $Re_p > 0$. Exemplary, the orientation-dependent drag coefficient $C_{D,\phi}$ is introduced next, and extended by drag correlations. The lift coefficient has been similarly derived and is summarized in the Appendix A.

The drag coefficient is defined by the relationship

$$C_{D,\phi} = C_{D,0} + (C_{D,90} - C_{D,0}) \sin^2\phi, \tag{7}$$

where $C_{D,0}$ and $C_{D,90}$ denote the values for the minimum and maximum inclination angles $\phi = 0^\circ$ and 90°. Although this relationship is an analytical solution for Stokes flow (Happel and Brenner, 2012), it is still accurate for higher particle Reynolds numbers (Sanjeevi and Padding, 2017). The drag coefficients for the limiting cases

$$C_{D,0} = C_{D,\text{Stokes},0}(Re_p, \beta) \cdot f_{d,0}(Re_p, \beta), \tag{8}$$

$$C_{D,90} = C_{D,\text{Stokes},90}(Re_p, \beta) \cdot f_{d,90}(Re_p, \beta), \tag{9}$$

are given by the analytical coefficients for Stokes flow $C_{D,\text{Stokes},0}$ and $C_{D,\text{Stokes},90}$. For $Re_p > 0$, the drag coefficient is scaled by empirical correlations $f_{d,0}(Re_p, \beta)$ and $f_{d,90}(Re_p, \beta)$. The full expressions $f_{d,0}(Re_p, \beta)$ and $f_{d,90}(Re_p, \beta)$ are summarized in the Appendix A.

The rotational particle dynamics are described by the particle angular velocity in the particle-fixed coordinate system $\widehat{\boldsymbol{\omega}}_p = \left(\omega_{p,\hat{x}}, \omega_{p,\hat{y}}, \omega_{p,\hat{z}}\right)$. The angular velocity of an ellipsoid subject to a fluid strain rate $\widehat{\boldsymbol{s}} = \left(s_{\hat{x}}, s_{\hat{y}}, s_{\hat{z}}\right)^T$ and a fluid angular velocity $\widehat{\boldsymbol{\omega}} = \left(\omega_{\hat{x}}, \omega_{\hat{y}}, \omega_{\hat{z}}\right)^T$ is described by

$$\begin{pmatrix} \frac{d\omega_{p,\hat{x}}}{dt} \\ \frac{d\omega_{p,\hat{y}}}{dt} \\ \frac{d\omega_{p,\hat{z}}}{dt} \end{pmatrix} = \begin{pmatrix} \omega_{p,\hat{y}}\omega_{p,\hat{z}} \frac{\beta^2-1}{1+\beta^2} \\ \omega_{p,\hat{z}}\omega_{p,\hat{x}} \frac{1-\beta^2}{1+\beta^2} \\ 0 \end{pmatrix} \tag{10}$$

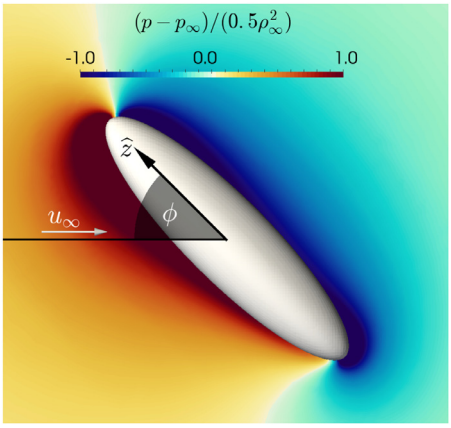

Fig. 2. Non-dimensional pressure distribution of an inclined ellipsoid in uniform flow with $Re_p = 5$, $\beta = 4$ and $\phi = 45^\circ$.

$$+ \frac{40}{9} \frac{\beta^{2/3}}{\tau_p} \begin{pmatrix} \frac{1}{\alpha_0 + \beta^2\gamma_0} \\ \frac{1}{\alpha_0 + \beta^2\gamma_0} \\ \frac{1}{2\alpha_0} \end{pmatrix} \begin{pmatrix} \frac{1-\beta^2}{1+\beta^2} s_{\hat{x}} + (\omega_{\hat{x}} - \omega_{p,\hat{x}}) \\ \frac{\beta^2-1}{1+\beta^2} s_{\hat{y}} + (\omega_{\hat{y}} - \omega_{p,\hat{y}}) \\ \omega_{\hat{z}} - \omega_{p,\hat{z}} \end{pmatrix}$$
$$+ \frac{5}{216} \frac{\rho_p}{\rho} \frac{Re_p^2}{\tau_p^2} \frac{C_{T,\phi}(Re_p, \beta)}{\beta^{-2/3} + \beta^{4/3}} \widehat{\boldsymbol{d}}_T.$$

The first two terms on the right-hand side are identical with the ellipsoidal Lagrangian model for Stokes flow. As for the translational dynamics, the rotational motion of the ellipsoids is fully governed by the flow field, the aspect ratio β, and the relaxation time τ_p, whereas the particle Reynolds number has no impact for $Re_p \to 0$. The last term is an extension of the hydrodynamic torque for $Re_p > 0$ to model the pitching torque due to fluid inertia.

To illustrate the direction of the pitching torque, Fig. 2 shows the non-dimensional pressure distribution of a uniform flow past an inclined ellipsoid for $Re_p = 5$, $\beta = 4$ and $\phi = 45^\circ$ which is one of the configurations studied in Fröhlich et al. (2020). Clearly, the pressure field is not fore-aft symmetric, and the high pressure regions on the windward side are not balanced by the low pressure regions on the leeward side. The net effect is a torque which pitches the ellipsoid towards the most stable orientation $\phi = 90^\circ$. For the pitching torque, the empirical torque coefficient

$$C_{T,\phi}(Re_p, \beta) = 2 \sin(\phi)\cos(\phi)\, C_{T,\max}(Re_p, \beta), \tag{11}$$

is used, where the maximum torque coefficient $C_{T,\max}(Re_p, \beta)$ is defined in the Appendix A. It vanishes for the extreme cases $\phi = 0^\circ$ or 90°, as well as for $\beta \to 1$. Note that the impact of the pitching torque on the orientation of the particles settling in a turbulent flow is essential in the current investigations.

In this study, the impact of the correlations for $Re_p > 0$ is investigated. Therefore, the ellipsoidal Lagrangian models are applied without and with the correlations. The Lagrangian model without the correlations is described in Siewert et al., 2014. It is also given by Eqs. (6) and (10), where the coefficients $C_{D,\phi}$ and $C_{L,\phi}$ are replaced by their expressions for $Re_p \to 0$ with $C_{T,\phi} = 0$. If the correlations are included in the Lagrangian model, the coefficients are set as defined in the Appendix A. Moreover, the equations for Stokes flow are fully governed by the flow field, the aspect ratio β, and the particle relaxation time τ_p. Specifically, the trajectories of particles with likewise aspect ratios and relaxation times are identically predicted in a one-way coupled Lagrangian framework. On the other hand, the drag correlations extend the set of equations by the particle Reynolds number as a further parameter.

The extension of the quasi-steady drag by correlations is only a correction for $Re_p > 0$. If compared to spherical particles, where mature dynamic equations exist, e.g., Maxey and Riley (1983),

additional contributions would be required for a more complete description. However, for the spherical case, these equations are mostly reduced to the dominating quasi-steady drag for $\rho_p \gg \rho$ and $d_{eq} < \eta$ (Kuerten, 2016), which is consistent with the chosen parameter configurations.

3. Computational setup

The conservation Eqs. 1 are solved via a cell-centered finite-volume discretization on Cartesian grids of second-order accuracy which has been described and thoroughly validated for compressible and nearly incompressible flows in a series of papers (Hartmann et al., 2011; Schneiders et al., 2013; 2016). An upwind-biased scheme is used to compute the inviscid fluxes and a central scheme is applied for the viscous fluxes, where the numerical dissipation is reduced by the reconstruction method of Thornber et al. (2008). The conservation equations are integrated in time using an explicit five-stage predictor-corrector Runge–Kutta method by Schneiders et al. (2016). For low Mach number, the time step size scales with the Mach number which is set $Ma = 0.1$ to achieve a larger computational time step with negligible compressibility effects. The ellipsoids are tracked using a Lagrangian framework similar to Siewert et al., 2014, where the fluid velocities and their gradients are interpolated at the particle positions via a third-order least-squares interpolation and the particle trajectories are integrated with a second-order accurate predictor-corrector scheme.

To ensure comparability to previous studies, the same generic configuration as in, e.g., Ferrante and Elghobashi (2003); Schneiders et al. (2017); Fröhlich et al. (2018) is considered as carrier flow, i.e., isotropic decaying turbulence in a fully periodic cube with the edge length L. The initial microscale Reynolds number is $Re_{\lambda 0} = u_0' \rho \lambda_0 / \mu = 79$, with the initial root-mean-square (rms) velocity u_0' and the initial Taylor microscale λ_0. Following Orszag, (1969), a divergence free random velocity field is initialized in spectral space. The initial energy spectrum is chosen $E(\kappa) = (3u_0'^2/2)(\kappa/\kappa_p^2)\exp(-\kappa/\kappa_p)$ as proposed by Schumann and Patterson (1978) with the base wavenumber $\kappa_0 = 2\pi/L$, and the peak wavenumber $\kappa_p = 4\kappa_0$. The flow field is directly resolved by 256^3 cells. The ellipsoids are injected at random positions and orientations. The particle velocity and angular velocity are initialized with the local fluid velocity and angular velocity at $t_i/t_{ref} = 0.28$ with the reference time $t_{ref} = u_0'^2/\epsilon_0$ and the initial dissipation rate ϵ_0. At this time, the velocity-derivative skewness converges to about -0.5 which indicates fully developed turbulent flow (Elghobashi and Truesdell, 1993).

Fig. 3 a illustrates the temporal development of the microscale Reynolds number Re_λ. After initialization, the microscale Reynolds number initially decays and then stays approximately constant within the range $31.5 < Re_\lambda < 34.5$ for $2 \leq t/t_{ref} \leq 4$. This time frame is used to gather the data for the statistics of the particle dynamics and orientations. Fig. 3b depicts the temporal development of the rms fluid velocity u' and the Kolmogorov velocity u_η scaled by the initial rms velocity u_0'. The non-dimensional temporal mean values for the statistically relevant time frame $2 \leq t/t_{ref} \leq 4$ denoted by the tilde symbol ~ are depicted for the rms velocity $\widetilde{u'}$ and the Kolmogorov velocity scale $\widetilde{u}_\eta$ by dashed lines. Fig. 3c and d show the temporal development of the ratio d_{eq}/η with the volume-equivalent diameter d_{eq} and the Stokes number based on the Kolmogorov time scale τ_k. The Stokes number in the statistically relevant time frame is chosen $\tau_p/\widetilde{\tau}_k = 1.23$ for all configurations and the diameter is set $d_{eq}/\widetilde{\eta} = 0.24$ with the density ratio $\rho_p/\rho = 400$. Note that the Stokes number is within the range where complex particle-turbulence interaction phenomena may be observed such as preferential concentration and preferential sweeping. These phenomena have been thoroughly analyzed for spherical particles in, e.g., Squires and Eaton (1991); Wang and Maxey (1993). While a detailed analysis for preferential concentration is beyond the scope of this study, statistical evidence on the impact of the correlations on the flow field experienced by the particles will be provided in Section 4.2

Table 1
Analyzed particle parameter space with the aspect ratio β, and the terminal velocity v_t scaled by the mean values of the rms velocity $\widetilde{u'}$, which have been gathered in the time frame $2 \leq t/t_{ref} \leq 4$. Additionally, the ratio $2c/\widetilde{\eta}$ of the major axis of the ellipsoid with respect to the Kolmogorov-length scale is provided.

β	2,	4,	8				
$v_t/\widetilde{u'}$	0.0,	0.25,	0.5,	1.0,	2.0,	3.0,	4.0
$2c/\widetilde{\eta}$	0.38,	0.60,	0.96				

The particle parameter space of the analyzed ellipsoids is summarized in Table 1. Simulations with all possible combinations of the aspect ratio β and the terminal velocity $v_t = \tau_p ||\boldsymbol{g}||$ defined by the particle relaxation time τ_p and gravity $\boldsymbol{g}$ acting in the $z-$direction are performed without and with the correlations.

To ensure converged statistics, 100,000 particles are tracked. The feedback of the particles on the flow field is not included to ensure a direct comparison between the particle response without and with the correlations on an identical flow field.

4. Results

First, the results of the ellipsoidal Lagrangian model without and with the correlations are compared for ellipsoidal particles settling in an isotropic decaying turbulent flow field. The analysis will focus on the impact of the novel drag correlations on the orientation of settling ellipsoidal particles. Subsequently, the particle Reynolds number effects are directly studied for varying particle diameters.

4.1. The impact of correlations on the orientation of settling ellipsoids

In the following, selected results for varying terminal velocities are presented. Although the quantitative results differ, a similar trend is true for all aspect ratios. Therefore, only the case $\beta = 4$ is presented.

Fig. 4 a shows the temporal development of the ensemble averaged particle Reynolds number $\langle Re_p \rangle$ for the cases $v_t/\widetilde{u'} = 0$ and $v_t/\widetilde{u'} = 4$. For a vanishing terminal velocity, the results are quite similar for the ellipsoidal Lagrangian model without and with the correlations. In this case, the rotational dynamics and the particle orientations are nearly identical (not shown). This can be explained by the relatively low mean particle Reynolds number with $\langle Re_p \rangle \leq 1$ and the isotropy of the flow field which tends to randomize the particle dynamics. For higher terminal velocities, the particle Reynolds numbers are higher and the impact of the correlations is quite significant for the $v_t/\widetilde{u'} = 4$ case. Nearly every statistical result of the particle dynamics is affected by the novel correlations for increasing particle terminal velocity. Exemplary, the temporal development of particle angular rms velocity is shown in Fig. 4b for $v_t/\widetilde{u'} = 4$. After injection of the particles, a sharp peak of the particle angular velocity can be observed for the results with correlations. Due to the high terminal velocity, the initially random oriented ellipsoids rapidly pitch towards an orientation where the pitching torque contribution and the torque due to the gradients are relatively balanced. After this initial peak, the particle angular velocity is slightly higher than the angular rms velocity of the fluid which is shown as a reference. The results of the Lagrangian model without correlations show an initially rapid decay and the angular

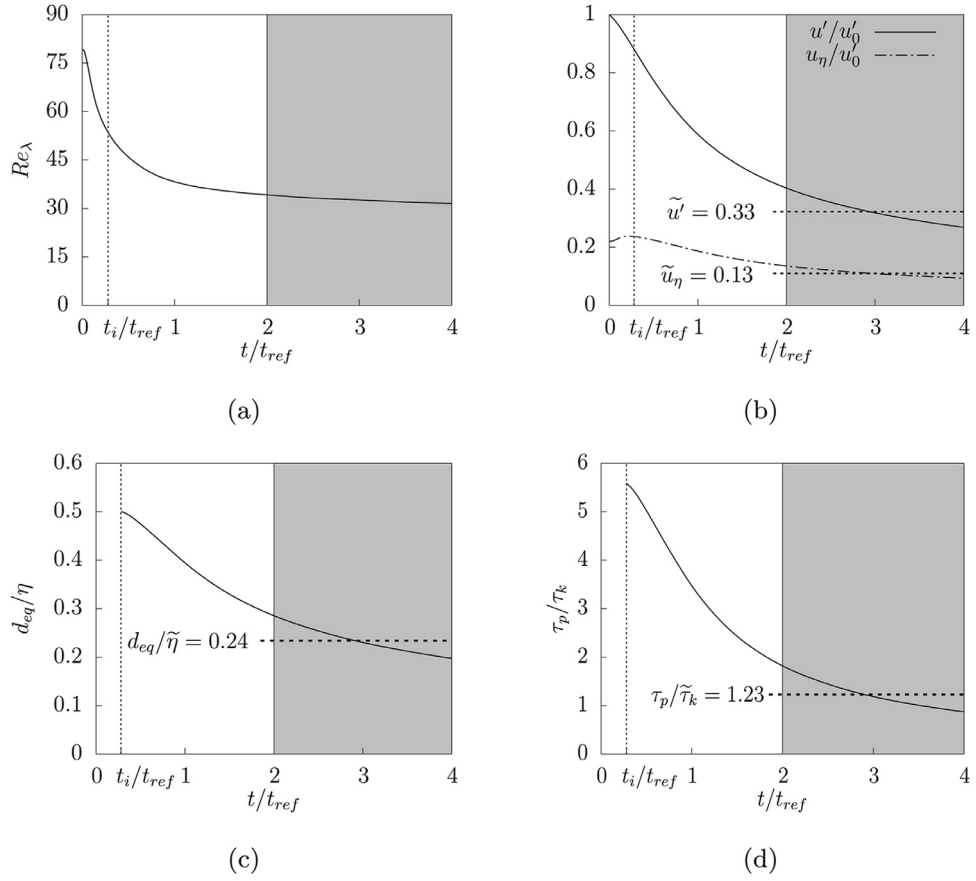

Fig. 3. Temporal development illustrated by solid lines of the Taylor Reynolds number Re_λ (a), the rms velocity of the fluid u' and the Kolmogorov velocity scale u_η non-dimensionalized by the initial rms velocity u'_0 (b), the ratio d_{eq}/η (c), and the Stokes number τ_p/τ_k (d). The particles are injected at $t_i/t_{ref} = 0.28$ and the particle statistics are averaged from $t/t_{ref} = 2.0$ to $t/t_{ref} = 4.0$. Non-dimensional average values of the fluid rms velocity $\widetilde{u}'$, the Kolmogorov velocity scale $\widetilde{u}_\eta$, the averaged diameter $d_{eq}/\widetilde{\eta}$, and the averaged Stokes number $\tau_p/\widetilde{\tau}_k$ are shown by dashed lines for this time frame.

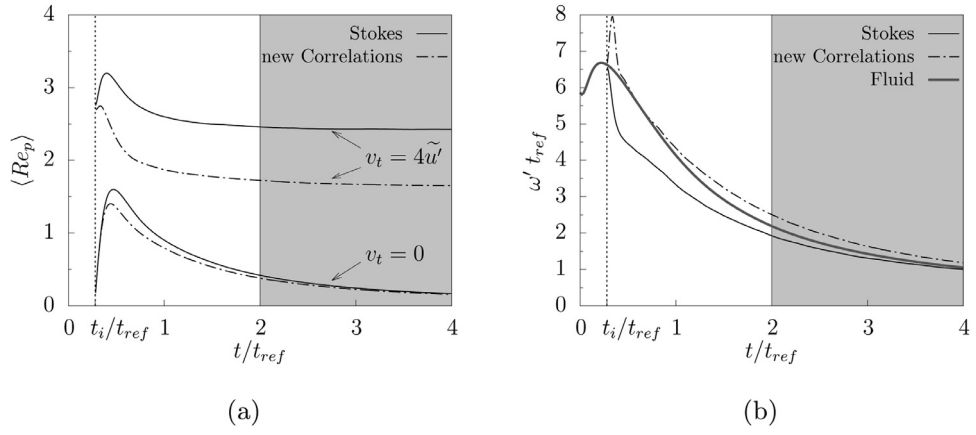

Fig. 4. Temporal development of the particle Reynolds number Re_p for the terminal velocities $v_t = 0$ and $v_t = 4\widetilde{u}'$(a), and the rms angular velocity of the particles for the $v_t = 4\widetilde{u}'$ case. The particle statistics of the results without and with correlations are compared. The fluid rms angular velocity is included in (b).

velocity is always statistically lower than the angular rms velocity of the fluid. Although the statistics of the rms value of the particle angular velocity partially converge, the overall dynamics of the ellipsoids are massively affected by the correlations.

Fig. 5 shows an instantaneous snapshot of the particle-laden turbulent flow field at $t/t_{ref} = 3.0$ for the case $v_t = \widetilde{u}'$ without and with the new correlations. The flow field is visualized by the second invariant of the velocity gradient tensor normalized by the mean enstrophy at that time, i.e., $Q/\langle 4\omega^2 \rangle$. Large vorticity dominated flow structures are colored in red and made opaque, whereas strain dominated regions are colored in gray and are made transparent. The ellipsoids are colored by the absolute orientation angle $\theta_z = \measuredangle(\hat{\boldsymbol{z}}, \boldsymbol{z})$ between the direction of their major axis $\hat{\boldsymbol{z}}$ and the direction of the terminal velocity $\boldsymbol{z}$.

The particle orientation of the Lagrangian model with the correlation (bottom) is clearly dominated by the pitching torque contribution and the particle orientation is close to the most stable orientation $\theta_z = 90^\circ$ for ellipsoids settling in a steady-state fluid. The orientation of the ellipsoid without the correlations (top) is clearly more scattered.

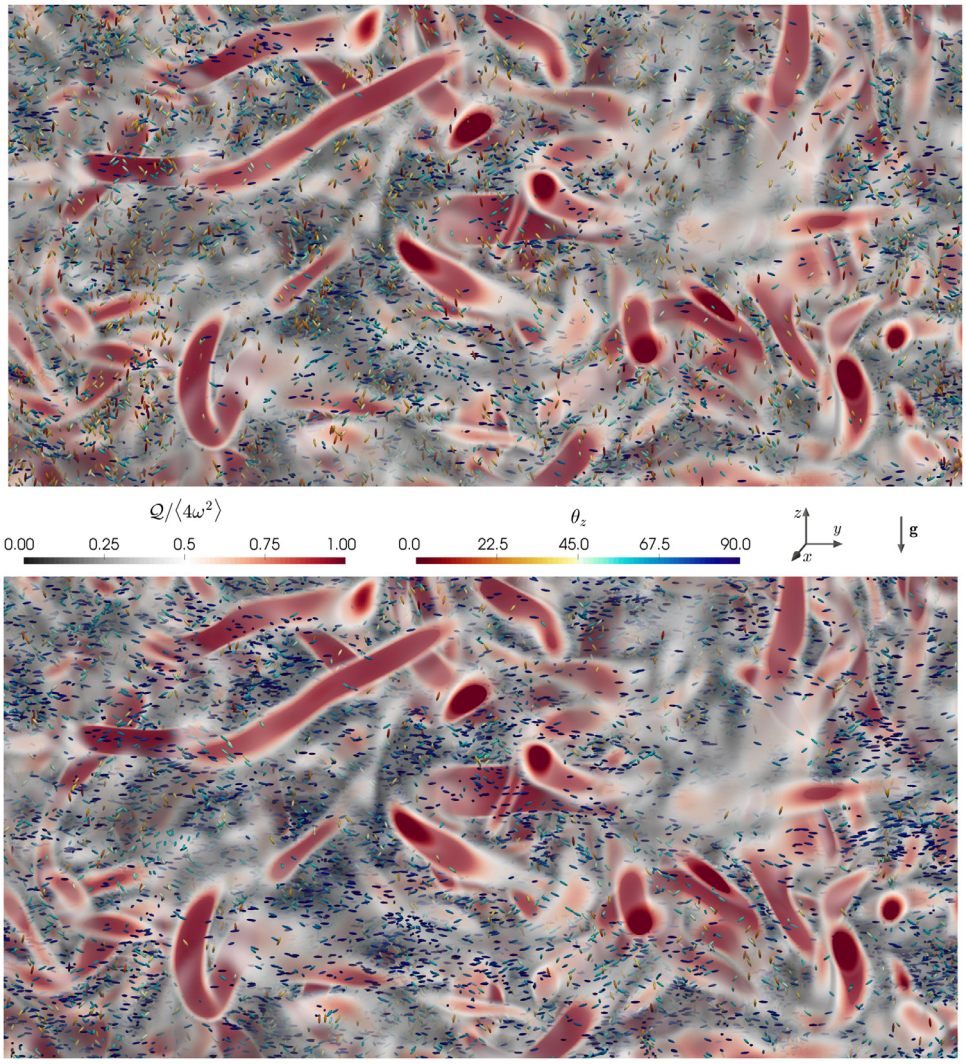

Fig. 5. Volume rendering of the second invariant of the velocity gradient tensor Q non-dimensionalized by the mean enstrophy $\langle 4\boldsymbol{\omega}\cdot\boldsymbol{\omega}\rangle = \langle 4\omega^2\rangle$ at $t/t_{ref} = 3.0$. The ellipsoidal particles for the case $\beta = 4$, $d_{eq}/\widetilde{\eta} = 0.24$, and $v_t = \widetilde{u'}$ are magnified by a factor of 3 and colored by their absolute orientation $\theta_z = \measuredangle(\hat{\boldsymbol{z}}, \boldsymbol{z})$ with respect to the direction of the terminal velocity $\boldsymbol{z}$. The results without/with correlations are shown at the top/bottom.

Following (Siewert et al., 2014), the orientation of the ellipsoids is statistically analyzed via the orientation distribution function (*odf*), i.e., the probability density function of the orientation scaled by the Jacobian $sin(\theta)$, where the θ bins are chosen such that they correspond to equal surface areas on the orientation sphere. Fig. 6 shows the *odf* of the angle between the particle major axis $\hat{\boldsymbol{z}}$ and the direction of the terminal velocity $\boldsymbol{z}$ without the correlations (a) and with the correlations (b). As expected, the particles are randomly oriented with respect to the $\boldsymbol{z}$ direction for a vanishing terminal velocity $v_t = 0$ with an *odf* value close to unity. The results of the ellipsoidal Lagrangian model without correlations shown in Fig. 6a indicate a preferential orientation of the ellipsoids where the major axis is aligned with the direction of the gravitational settling for increasing terminal velocities. The opposite effect can be observed for the results with the correlations in Fig. 6b. The ellipsoids are preferably oriented with their major axis perpendicular to the direction of the gravitational settling. This trend increases for higher terminal velocities.

The opposite predictions of the orientation without and with correlations shown in Fig. 6 are in agreement with the findings in several studies referred to in the Introduction. That is, the alignment of the major axis of the ellipsoidal particles with the gravitational settling direction is consistent with previous studies using the Lagrangian model without correlations (Challabotla et al., 2016; Siewert et al., 2014). The opposite behavior was observed using analytical expansions for low but finite Re_p. Estimates for nearly spherical particles in Klett (1995) and for arbitrary particles (Sheikh et al., 2020) indicate a dominance of the torque contributions due to fluid inertia effects over the velocity gradients in isotropic turbulence. Although the results cannot be directly compared due to different numerical setups, the current data with correlations support the findings by van Wachem et al. (2015), where the ellipsoidal particles showed a pronounced preference for relatively high inclination angles in a horizontal channel flow with wall-normal gravity. However, the alignment of the major axis with the gravitational settling as shown in Arcen et al. (2017) for ellipsoidal particles in vertical channel flow with wall-parallel gravity can not be observed for any configuration with correlations in the current study. Further studies of particle-laden turbulent wall-bounded flows would be required with horizontal and vertical configurations to fully resolve the apparently conflicting results.

Although the pitching torque contribution due to the fluid inertia dominates the rotational particle dynamics, the contributions due to the velocity gradients can not be neglected for an accurate prediction of the rotational particle dynamics. The spinning rate, i.e., the rotational rate aligned with the major axis of the ellip-

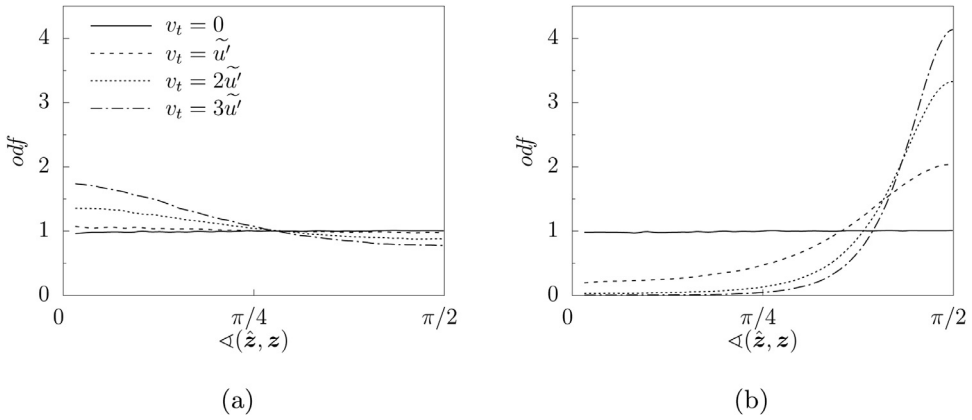

Fig. 6. Orientation distribution function (*odf*) of the particle orientation with respect to the direction of the terminal direction $\sphericalangle(\hat{\boldsymbol{z}}, \boldsymbol{z})$ for various terminal velocities. The results without/with correlations are shown in (a)/(b).

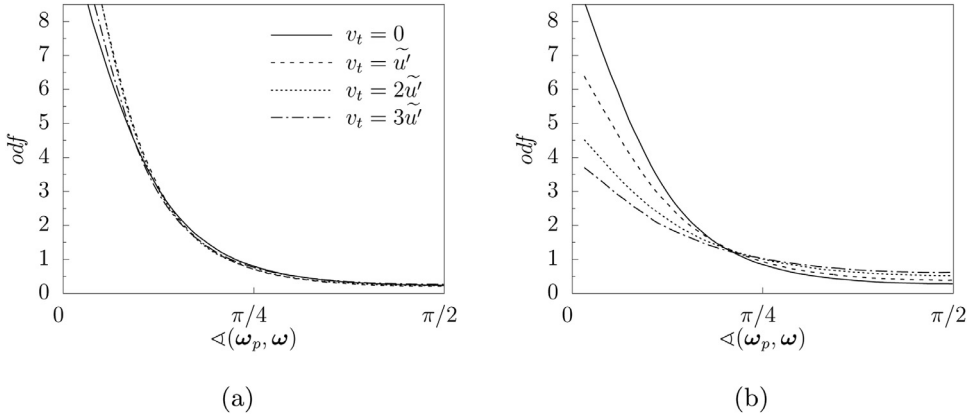

Fig. 7. Alignment of the particle angular velocity $\boldsymbol{\omega}_p$ with the fluid angular velocity $\sphericalangle(\boldsymbol{\omega}_p, \boldsymbol{\omega})$ without/with correlations are shown in (a)/(b) for various particle terminal velocities.

soid, is not directly affected by the pitching torque which is by definition perpendicular to the major axis. Moreover, the pitching torque vanishes for high and low inclination angles. Fig. 7 shows the alignment of the particle angular velocity with the local fluid angular velocity for several terminal velocities. The distributions of the Lagrangian model without correlations in Fig. 7(a) yield a particle rotation which is strongly aligned with the local angular velocity almost independent from the terminal velocity. If the correlations are included in Fig. 7(b), similar results are obtained for $v_t = 0$, whereas the alignment is strongly reduced for increasing terminal velocities. Nevertheless, even for the relatively high terminal velocity $v_t = 3\widetilde{u}'$ a certain alignment of the particle rotation remains.

4.2. Reynolds number effects on settling ellipsoids

As described in Section 2.2, the results of the conventional ellipsoidal Lagrangian model without correlations are fully determined by the flow field, the aspect ratio, and the particle relaxation time. It has to be emphasized that the particle Reynolds number has no impact on the particle trajectories since the model was derived for $Re_p \to 0$.

In the following, the Reynolds number effects are directly quantified by an additional set of simulations. That is, all parameter combinations listed in Table 1 and analyzed in the previous setup for $d_{eq}/\widetilde{\eta} = 0.24$ and $\rho_p/\rho = 400$ are extended by the cases $d_{eq}/\widetilde{\eta} = 0.12$ and $\rho_p/\rho = 1600$, as well as $d_{eq}/\widetilde{\eta} = 0.48$ and $\rho_p/\rho = 100$. The particle relaxation time and the Stokes number $\tau_p/\widetilde{\tau}_k = 1.23$ remains constant for all diameter and density combinations. Consequently, the results of the Lagrangian model without correlations are identical to the case $d_{eq}/\widetilde{\eta} = 0.24$ and $\rho_p/\rho = 400$. If the correlations are included, the results are different for each diameter-density combination since the particle Reynolds number changes. More precisely, the drag force in Eq. (6) scales with the drag correction functions $f_{d,0}$ and $f_{d,90}$ and the pitching torque contribution in Eq. (10) scales with $C_{T,\phi}(Re_p, \beta)$. The exact formulations of the drag correction functions and the torque coefficient are listed in the Appendix A. The ratio $2c/\widetilde{\eta}$ of the major axis of the ellipsoid to the Kolmogorov-length scale is within the limits 0.19 and 1.92. The upper value is at the applicability limit of the ellipsoidal Lagrangian model. This length-scale ratio is within the range where non-linear variations of the flow field are possible (Voth and Soldati, 2017). However, only moderate statistical deviations of the Lagrangian model have been observed for a similar range in Ravnik et al., 2018 for a turbulent channel flow.

Fig. 8 shows the ratio of the mean settling velocity obtained with the correlations $\widetilde{v}_{t,c}$ over the mean settling velocity obtained without the correlations, i.e., based on Stokes flow, $\widetilde{v}_{t,s}$ for varying terminal velocities and $\beta = 2$ and $\beta = 8$. All results have been obtained for an identical particle relaxation time. Clearly, the correlations have a massive impact on the mean settling velocity. As presented in the previous Section, the pitching torque contributions dominate the torque contributions by the velocity gradients especially for higher terminal velocities. Additionally, the drag correction function further increases the predicted drag for higher inclination angles. For $\phi = 90°$, the drag correction function $f_{d,90}$ is relatively high even for moderate particle Reynolds numbers.

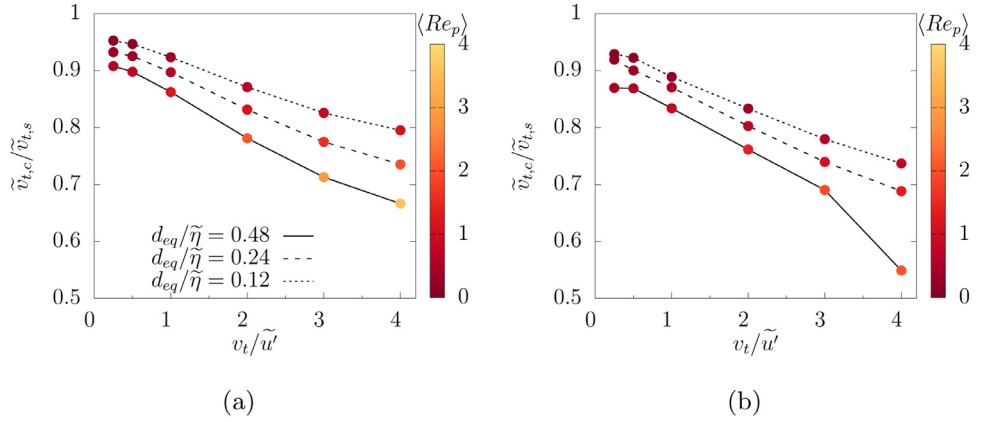

Fig. 8. Ratio of the mean settling velocity of the ellipsoids simulated with the correlations $\widetilde{v}_{t,c}$ and without the correlations $\widetilde{v}_{t,s}$ for various settling velocities v_t. The color of the data points indicates the mean particle Reynolds number $\langle Re_p \rangle$. The results are presented for three diameters and $\beta = 2$ in (a) and $\beta = 8$ in (b).

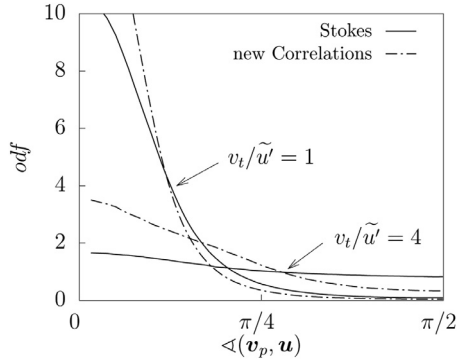

Fig. 9. Alignment of the particle velocity $\boldsymbol{v}_p$ with the fluid velocity at the particle position $\boldsymbol{u}$ for $\beta = 8$, $d_{eq}/\widetilde{\eta} = 0.48$ for the cases $v_t/\widetilde{u}' = 1$ and $v_t/\widetilde{u}' = 4$.

The data points shown in Fig. 8 are colored by the mean particle Reynolds numbers. The lowest ratio $\widetilde{v}_{t,c}/\widetilde{v}_{t,s} = 0.54$ can be observed for the parameter combination $v_t = 4\widetilde{u}'$, $\beta = 8$ and $d_{eq}/\widetilde{\eta} = 0.47$ in Fig. 8b with a mean particle Reynolds number $\langle Re_p \rangle = 2$. The corresponding drag coefficient is $f_{d,90}(Re_p = 2, \beta = 8) = 1.42$. The combination of a much higher inclination angle and a significantly high drag correction function yields a high drag force and explains the huge difference between the results without and with correlations.

The decreased settling velocity affects the response of the particles on the turbulent fluctuations which will be analyzed in the following for $\beta = 8$, $d_{eq}/\widetilde{\eta} = 0.48$. Fig. 9 shows a comparison of the alignment of the particle velocity with the fluid velocity predicted by the Lagrangian model without correlations against the results with correlations for the settling velocities $v_t/\widetilde{u}' = 1$ and $v_t/\widetilde{u}' = 4$. Due to the decreased settling velocities predicted by the Lagrangian model with the correlations, the particles have more time to respond to the turbulent fluctuations which leads to an enhanced alignment especially for $v_t/\widetilde{u}' = 4$.

Fig. 10 shows the *pdf* of the fluid velocity in settling direction $\widetilde{u}_z$ experienced by the particles. For a direct comparison of upward and downward motion, the absolute values are visualized for $\widetilde{u}_z < 0$, i.e., the color indicates the sign of the fluid velocity. The settling particles are preferentially sampling downward fluid motion which is referred to as preferential sweeping (Wang and Maxey, 1993). Fig. 10a shows that this effect of particle-turbulence interaction is identically predicted by the Lagrangian model without and with the correlations for $v_t/\widetilde{u}' = 1$. Analogous to the findings of Wang and Maxey (1993) for spherical particles, the preferential sweeping decreases if the terminal velocity is further increased since the particles have less time to react on the turbulent fluctuations due to their inertia. Fig. 10b shows that for $v_t/\widetilde{u}' = 4$, the Lagrangian model without correlations predicts only a vanishing tendency towards a preferred downward fluid motion. If the correlations are included, preferential sweeping can be clearly observed.[Rev#1]

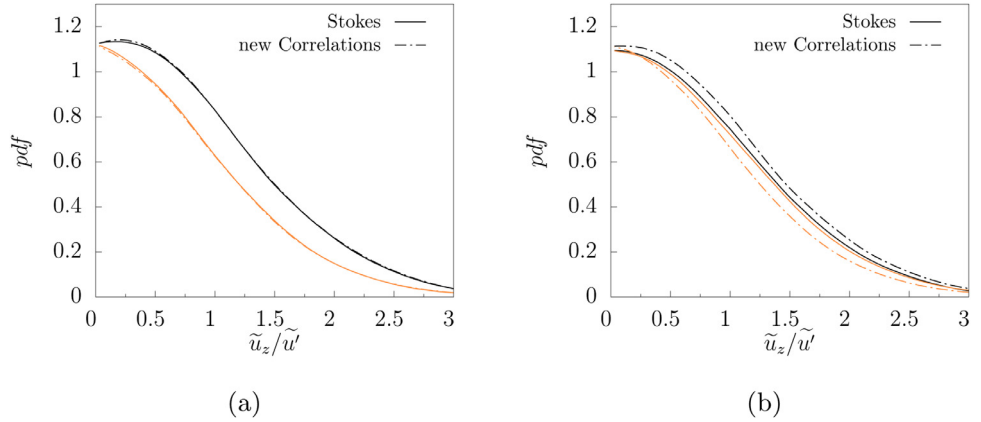

Fig. 10. Probability density function (*pdf*) of the fluid velocity at the particle position in settling direction $\widetilde{u}_z$ with $\beta = 8$, $d_{eq}/\widetilde{\eta} = 0.48$ for $v_t/\widetilde{u}' = 1$ (a) and $v_t/\widetilde{u}' = 4$ (b). Absolute values are depicted for $\widetilde{u}_z < 0$ by black lines, whereas the orange lines indicate $\widetilde{u}_z > 0$.

5. Summary

Fluid inertia effects on the dynamics of ellipsoidal particles settling in isotropic decaying turbulence are analyzed where the flow field is directly resolved. Therefore, a popular point-particle model based on Jeffery's equations for ellipsoidal particle dynamics in viscous shear flow is reformulated to include drag and lift coefficients. The results of the point-particle model without correlations for $Re_p > 0$ are compared against the results based on recently developed drag, lift, and torque correlations by Fröhlich et al. (2020) which are included in the point-particle model. In total, 126 simulations are conducted to assess the impact of the correlations regarding the aspect ratio, the terminal velocity, and the particle Reynolds number. Although the mean particle Reynolds number remains quite moderate, i.e., $\langle Re_p \rangle \leq 4$, for all configurations, the correlations have a significant impact on the particle dynamics.

The pitching torque contribution due to fluid inertia effects, which is modeled by correlations, leads to a preferential orientation of the particles. The particles are mostly oriented with their major axis perpendicular to the settling direction. This is in contrast to the results of the Lagrangian model without the correlations which show an alignment of the major axis with the settling direction. This observation is in agreement with the results of Sheikh et al. (2020) based on leading order expansions. However, since the pitching torque vanishes for inclination angles $\phi \to 90^\circ$, the particle angular velocity is still aligned with the local angular velocity of the fluid.

Next, Reynolds number effects are studied via a set of simulations for varying particle diameters at constant particle relaxation time. For these configurations, the results of the Lagrangian model without the correlations remain identical, whereas the results with correlations are affected by a modified particle Reynolds number. The combination of drag correction functions and altered particle orientations yields a massive impact of the correlations on the settling velocity of the ellipsoidal particles. For the most pronounced case, the settling velocity was reduced by 46% compared to the results without correlations. The decreased settling velocity leads to enhanced preferential sweeping since the particle have more time to react on the turbulent fluctuations.

These results show that the correlations have to be included in the ellipsoidal Lagrangian model and the particle Reynolds number has to be considered an additional parameter in the setup of a multiphase system even for relatively low particle Reynolds numbers. However, a validation against fully-resolved particle-laden simulations like in Fröhlich et al. (2018) for spherical particles would be required to determine whether the relatively simple extension of the ellipsoidal Lagrangian model for Stokes flow by correlations for $Re_p > 0$ is sufficiently accurate.

Declaration of Competing Interest

The authors declare that they have no known competing financial interests or personal relationships that could have appeared to influence the work reported in this paper.

CRediT authorship contribution statement

Konstantin Fröhlich: Conceptualization, Methodology, Investigation, Writing - original draft. **Pooria Farmand:** Writing - review & editing. **Heinz Pitsch:** Supervision, Project administration. **Matthias Meinke:** Software, Resources, Data curation. **Wolfgang Schröder:** Writing - review & editing, Supervision, Funding acquisition.

Acknowledgments

This work has been funded by the German Research Foundation (DFG) within the framework of the SFB/Transregio 129 'Oxyflame'. The support is gratefully acknowledged. Computing resources were provided by the High Performance Computing Center Stuttgart (HLRS) and by the Jülich Supercomputing Centre (JSC) within a Large-Scale Project of the Gauss Centre for Supercomputing (GCS).

Appendix A

The drag coefficients $C_{D,0}$ and $C_{D,90}$, the lift coefficient $C_{L,\phi}$, and the torque coefficient $C_{T,\phi}$ required for the Lagrangian model rely on empirical expressions derived in Fröhlich et al. (2020) which are briefly summarized in the following.

The drag coefficients for Stokes flow

$$C_{D,\mathrm{Stokes},0}(Re_p,\beta) = \frac{64\beta^{2/3}}{Re_p}\frac{1}{\chi_0/a^2+\beta^2\gamma_0}, \qquad (12)$$

$$C_{D,\mathrm{Stokes},90}(Re_p,\beta) = \frac{64\beta^{2/3}}{Re_p}\frac{1}{\chi_0/a^2+\alpha_0},$$

are defined by the shape parameters α_0, χ_0, and γ_0 given in Table 2. They are corrected by the empirical functions

$$f_{d,0}(Re_p,\beta) = 1 + 0.15Re_p^{0.687} + c_{d,1}(\log\beta)^{c_{d,2}}Re_p^{c_{d,3}+c_{d,4}\log\beta}, \qquad (13)$$

$$f_{d,90}(Re_p,\beta) = 1 + 0.15Re_p^{0.687} + c_{d,5}(\log\beta)^{c_{d,6}}Re_p^{c_{d,7}+c_{d,8}\log\beta}. \qquad (14)$$

in Eq. (8).

For Stokes flow, the lift coefficient is defined by Happel and Brenner (2012) as

$$C_{L,\mathrm{Stokes},\phi}(Re_p,\beta) = 2\sin(\phi)\cos(\phi)\, C_{L,\mathrm{Stokes,max}}(Re_p,\beta) \qquad (15)$$

with the maximum lift coefficient at $\phi = 45^\circ$

$$C_{L,\mathrm{Stokes,max}}(Re_p,\beta) = \frac{C_{D,\mathrm{Stokes},90}(Re_p,\beta) - C_{D,\mathrm{Stokes},0}(Re_p,\beta)}{2}. \qquad (16)$$

For $Re_p > 0$, Eq. (15) does not hold and the expression is replaced by

$$C_{L,\phi}(Re_p,\beta) = 2\sin(\psi_\phi(Re_p,\beta))\cos(\psi_\phi(Re_p,\beta))\, C_{L,\max}(Re_p,\beta) \qquad (17)$$

with the empirical coordinate transformation $\psi_\phi(Re_p,\beta)$

$$\psi_\phi(Re_p,\beta) = \frac{\pi}{2}\left(\frac{\phi}{\pi/2}\right)^{f_{l,shift}(Re_p,\beta)}, \qquad (18)$$

$$f_{l,shift}(Re_p,\beta) = \begin{cases} 1 + c_{l,1}(\log\beta)^{c_{l,2}}(\log Re_p)^{c_{l,3}}, & Re_p > 1 \\ 1, & \text{otherwise.} \end{cases} \qquad (19)$$

Table 2
Analytical shape coefficients for prolate ellipsoids with $\beta > 1$.

χ_0	α_0	γ_0	κ
$\frac{-a^2\beta}{\sqrt{\beta^2-1}}\kappa$	$\frac{\beta^2}{\beta^2-1} + \frac{\beta}{2(\beta^2-1)^{3/2}}\kappa$	$-\frac{2}{\beta^2-1} - \frac{\beta}{(\beta^2-1)^{3/2}}\kappa$	$\log\left(\frac{\beta-\sqrt{\beta^2-1}}{\beta+\sqrt{\beta^2-1}}\right)$

Table 3
Empirical parameters for the drag, lift, and torque correlations.

	$i=1$	$i=2$	$i=3$	$i=4$	$i=5$	$i=6$	$i=7$	$i=8$
$c_{d,i}$	−0.007	1.0	1.17	−0.07	0.047	1.14	0.7	−0.008
$c_{l,i}$	0.01	0.86	1.77	0.34	0.88	−0.05	–	–
$c_{t,i}$	0.931	0.675	0.162	0.657	2.77	0.178	0.177	–

The maximum lift coefficients is corrected for $Re_p > 0$ by

$$C_{L,\max}(Re_p, \beta) = f_{l,\max}(Re_p, \beta)\, C_{L,\text{Stokes},\max}(Re_p, \beta) \tag{20}$$

with an empirical correction function

$$f_{l,\max}(Re_p, \beta) = 1 + c_{l,4} Re_p^{c_{l,5}+c_{l,6}\log\beta}. \tag{21}$$

The empirical torque coefficient which describes the pitching torque acting on an inclined ellipsoid is defined by

$$C_{T,\max}(Re_p, \beta) = \frac{c_{t,1}(\log\beta)^{c_{t,2}}}{Re_p^{c_{t,3}}} + \frac{c_{t,4}(\log\beta)^{c_{t,5}}}{Re_p^{c_{t,6}+c_{t,7}\log\beta}}. \tag{22}$$

The empirical parameters for the drag, lift, and torque correlations $c_{d,i}$, $c_{l,i}$, and $c_{t,i}$, based on the results of 4,400 highly resolved simulations are listed in Table 3. The correlations are valid for $Re_p \leq 100$.

References

Andersson, H.I., Jiang, F., 2019. Forces and torques on a prolate spheroid: low-Reynolds-number and attack angle effects. Acta Mech. 230 (2), 431–447.

Arcen, B., Ouchene, R., Khalij, M., Tanière, A., 2017. Prolate spheroidal particles' behavior in a vertical wall-bounded turbulent flow. Phys. Fluids 29 (9), 093301.

Aris, R., 2012. Vectors, Tensors and the Basic Equations of Fluid Mechanics. Dover Publications.

Balachandar, S., Eaton, J.K., 2010. Turbulent dispersed multiphase flow. Annu. Rev. Fluid Mech. 42, 111–133.

Challabotla, N.R., Zhao, L., Andersson, H.I., 2016. On fiber behavior in turbulent vertical channel flow. Chem. Eng. Sci. 153, 75–86.

Cox, R.G., 1965. The steady motion of a particle of arbitrary shape at small Reynolds numbers. J. Fluid Mech. 23 (4), 625–643.

Dabade, V., Marath, N.K., Subramanian, G., 2015. Effects of inertia and viscoelasticity on sedimenting anisotropic particles. J. Fluid Mech. 778, 133–188.

Elghobashi, S., Truesdell, G.C., 1993. On the two-way interaction between homogeneous turbulence and dispersed solid particles. I: turbulence modification. Phys. Fluids A 5 (7), 1790–1801.

Ferrante, A., Elghobashi, S., 2003. On the physical mechanisms of two-way coupling in particle-laden isotropic turbulence. Phys. Fluids 15 (2), 315–329.

Fröhlich, K., Meinke, M., Schröder, W., 2020. Correlations for inclined prolates based on highly resolved simulations. J. Fluid Mech. 901, A5.

Fröhlich, K., Schneiders, L., Meinke, M., Schröder, W., 2018. Validation of Lagrangian two-way coupled point-particle models in large-eddy simulations. Flow Turbul. Combust. 101 (2), 317–341.

Gustavsson, K., Sheikh, M.Z., Lopez, D., Naso, A., Pumir, A., Mehlig, B., 2019. Effect of fluid inertia on the orientation of a small prolate spheroid settling in turbulence. New J. Phys. 21 (8), 083008.

Happel, J., Brenner, H., 2012. Low Reynolds Number Hydrodynamics: With Special Applications to Particulate Media. Springer.

Hartmann, D., Meinke, M., Schröder, W., 2011. A strictly conservative Cartesian cut–cell method for compressible viscous flows on adaptive grids. Comput. Methods Appl. Mech. Eng. 200 (9-12), 1038–1052.

Jeffery, G.B., 1922. The motion of ellipsoidal particles immersed in a viscous fluid. Proc. R. Soc. A 102 (715), 161–179.

Khayat, R.E., Cox, R.G., 1989. Inertia effects on the motion of long slender bodies. J. Fluid Mech. 209, 435–462.

Klett, J.D., 1995. Orientation model for particles in turbulence. J. Atmos. Sci. 52 (12), 2276–2285.

Kuerten, J.G.M., 2016. Point-particle DNS and LES of particle-laden turbulent flow - a state-of-the-art review. Flow Turbul. Combust. 97 (3), 689–713.

Lopez, D., Guazzelli, E., 2017. Inertial effects on fibers settling in a vortical flow. Phys. Rev. Fluids 2 (2), 024306.

Marchioli, C., Soldati, A., 2013. Rotation statistics of fibers in wall shear turbulence. Acta Mech. 224 (10), 2311–2329.

Marchioli, c., Zhao, L., Andersson, H.I., 2016. On the relative rotational motion between rigid fibers and fluid in turbulent channel flow. Phys. Fluids 28 (1), 013301.

Maxey, M.R., Riley, J.J., 1983. Equation of motion for a small rigid sphere in a nonuniform flow. Phys. Fluids 26 (4), 883–889.

Mortensen, P.H., Andersson, H.I., Gillissen, J.J.J., Boersma, B.J., 2008. On the orientation of ellipsoidal particles in a turbulent shear flow. Int. J. Multiph. Flow 34 (7), 678–683.

Orszag, S.A., 1969. Numerical methods for the simulation of turbulence. Phys. Fluids 12 (12), II–250.

Ouchene, R., Khalij, M., Arcen, B., Tanière, A., 2016. A new set of correlations of drag, lift and torque coefficients for non-spherical particles and large Reynolds numbers. Powder Tech. 303, 33–43.

Ravnik, J., Marchioli, C., Soldati, A., 2018. Application limits of Jeffery's theory for elongated particle torques in turbulence: a DNS assessment. Acta Mech. 229 (2), 827–839.

Roy, A., Hamati, R.J., Tierney, L., Koch, D.L., Voth, G.A., 2019. Inertial torques and a symmetry breaking orientational transition in the sedimentation of slender fibres. J. Fluid Mech. 875, 576–596.

Sanjeevi, S.K.P., Padding, J.T., 2017. On the orientational dependence of drag experienced by spheroids. J. Fluid Mech. 820, R1.

Schneiders, L., Fröhlich, K., Meinke, M., Schröder, W., 2019. The decay of isotropic turbulence carrying non-spherical finite-size particles. J. Fluid Mech. 875, 520–542.

Schneiders, L., Günther, C., Meinke, M., Schröder, W., 2016. An efficient conservative cut-cell method for rigid bodies interacting with viscous compressible flows. J. Comput. Phys. 311, 62–86.

Schneiders, L., Hartmann, D., Meinke, M., Schröder, W., 2013. An accurate moving boundary formulation in cut-cell methods. J. Comput. Phys. 235, 786–809.

Schneiders, L., Meinke, M., Schröder, W., 2017. Direct particle-fluid simulation of Kolmogorov-length-scale size particles in decaying isotropic turbulence. J. Fluid Mech. 819, 188–227.

Schumann, U., Patterson, G.S., 1978. Numerical study of pressure and velocity fluctuations in nearly isotropic turbulence. J. Fluid Mech. 88 (4), 685–709.

Sheikh, M.Z., Gustavsson, K., Lopez, D., Mehlig, B., Pumir, A., Naso, A., 2020. Importance of fluid inertia for the orientation of spheroids settling in turbulent flow. J. Fluid Mech. 886, A9.

Siewert, C., Kunnen, R.P.J., Meinke, M., Schröder, W., 2014. Orientation statistics and settling velocity of ellipsoids in decaying turbulence. Atmos. Res. 142, 45–56.

Squires, K.D., Eaton, J.K., 1991. Preferential concentration of particles by turbulence. Phys. Fluids A 3 (5), 1169–1178.

Thornber, B., Mosedale, A., Drikakis, D., Youngs, D., Williams, R., 2008. An improved reconstruction method for compressible flows with low Mach number features. J. Comput. Phys. 227 (10), 4873–4894.

van Wachem, B., Zastawny, M., Zhao, F., Mallouppas, G., 2015. Modelling of gas–solid turbulent channel flow with non-spherical particles with large Stokes numbers. Int. J. Multiph. Flow 68, 80–92.

Voth, G.A., Soldati, A., 2017. Anisotropic particles in turbulence. Annu. Rev. Fluid Mech. 49, 249–276.

Wang, L.-P., Maxey, M.R., 1993. Settling velocity and concentration distribution of heavy particles in homogeneous isotropic turbulence. J. Fluid Mech. 256, 27–68.

White, F.M., 1991. Viscous Fluid Flow. McGraw-Hill.

Zastawny, M., Mallouppas, G., Zhao, F., van Wachem, B., 2012. Derivation of drag and lift force and torque coefficients for non-spherical particles in flows. Int. J. Multiph. Flow 39, 227–239.